Linking Solidification Dynamics And Intermetallic Evolution To The Machinability Of A Multicomponent Al-Cu-Ni-Ta Alloy

André Cruz da Costa Maciel[1*], Héricles Ruiliman Oliveira de Souza[1], Wellington Bruno Silva de Jesus[2], Maria Adrina Paixão de Souza da Silva[1]

[1]Graduate Program in Mechanical Engineering (PPGEM), Federal University of Pará (UFPA), Belém, Pará, Brazil.
[2]Graduate Program in Materials Science and Engineering (PPGCEM), Military Institute of Engineering (IME), Rio de Janeiro, Rio de Janeiro, Brazil.

Abstract

The present work investigates the coupled effects of thermal solidification parameters and microstructural evolution on the machinability of a Al-33%Cu-1%Ni-1.2%Ta weight, solidified under transient upward directional solidification. Solidification kinetics, macro and microstructural characterization, and quantitative analysis of secondary dendritic arm spacing (λ_2), eutectic lamellar spacing, and complex intermetallic morphologies were conducted along the length of the ingot. A consistent pathway was identified for the evolution of intermetallics containing Ta and Ni, showing position-dependent transformations from Al_3Ta and $Al_2$to Ni_3Ta/Ta(,Al)$_2$ with $Al_{74}Ni$ rims. Machinability tests revealed shear temperatures of up to approximately 44 °C at a distance of 40 mm from the cold. Oscillating heating rates were observed in the columnar-equiaxial transition zone (*CET*). The maximum flank wear reached 0.071 mm, which is well below the *ISO* 3685 limit, while the surface roughness decreased from 0.27 μm near cold to 0.17 μm in the equiaxial region. Chip morphology has evolved from predominantly arc-shaped near cold to mixed arc/needle types in the *CET* and equiaxial zones. Multivariate regression identified liquidus isotherm velocity (V_L) as the most influential variable on machinability responses, followed by cooling rate (T_R), while λ_2 and specific intermetallic fractions played secondary roles. This is the first demonstration that the coupled solidification path of quaternary Al-Ni-Ta alloys governs position-dependent machinability. These findings provide new insights for tooling design, process optimization, and the sustainable use of complex aluminum alloys in advanced manufacturing.

Keywords: Aluminum alloys; directional solidification; intermetallic compounds; turning operation; multivariate regression analysis.

Highliths

- Integrated analysis of solidification parameters, intermetallic evolution, and machinability in an Al-33wt.%Cu-1wt.%Ni-1.2wt.%Ta alloy.

- Defined transformation pathway of Ta- and Ni-bearing intermetallics under transient cooling conditions.
- Quantitative correlations between λ_2, eutectic/intermetallic metrics, and machinability responses.
- Identification of the *CET* region as the critical zone for wear and thermal instability during machining.
- Industrial relevance: results support microstructure-based strategies to improve machinability of high-strength aluminum alloys.

I. INTRODUCTION

Aluminum is widely recognized for its outstanding combination of properties, including a high strength-to-weight ratio, excellent malleability, high thermal and electrical conductivity, corrosion resistance, and full recyclability. These attributes, combined with the versatility of manufacturing processes such as casting, rolling, extrusion, and machining, make aluminum an essential material across a broad range of applications, from industrial structures to aerospace, transportation, and biomedical components [1-3].

Among aluminum alloys, cast alloys of the 2XX.X series, primarily alloyed with copper and often containing significant amounts of magnesium, silicon, nickel, and tantalum, are notable for their high mechanical strength, especially after heat treatment. However, these alloys typically exhibit lower corrosion resistance and formability compared to other aluminum alloy families [4, 5]. The addition of Ni and Ta can lead to the formation of complex intermetallic phases, with a direct impact on both the mechanical and thermal behavior of the material [6, 7].

The machining performance of these alloys is significantly influenced by their microstructural features, which are determined during the solidification process. Parameters such as grain morphology, dendritic spacings, and phase distribution are closely linked to the solidification route employed. Under directional solidification, particularly in a transient heat extraction regime, thermal parameters such as the cooling rate (T_R) and liquidus isotherm velocity (V_L) play a decisive role in microstructural refinement and, consequently, in the machinability of the material [8 - 11].

Machining remains one of the most critical manufacturing processes in the metal-mechanical industry due to its versatility and precision. Machinability, defined as the relative ease with which a material can be cut, is not an intrinsic property, but rather the outcome of complex interactions among material properties, tool geometry and composition, cutting parameters, and the use of cutting fluids. Common evaluation

criteria include cutting temperature, tool wear, surface roughness, and chip morphology [8 - 11].

Despite the extensive literature on machinability, relatively few studies have addressed the combined influence of manufacturing route, solidification conditions, and the resulting microstructure on machining performance [12 - 14], particularly for complex alloys such as Al-Cu-Ni-Ta [15]. A systematic investigation integrating these aspects can provide valuable insights for the development of materials tailored for subtractive manufacturing processes, enabling cost reduction and improved component reliability.
The application of multivariate regression analysis to correlate solidification parameters with machinability criteria is scarce, not to mention absent in the literature. Most studies addressing the machining behavior of metallic alloys focus on individual microstructural parameters or isolated thermal conditions, without establishing a comprehensive statistical relationship between the complex set of variables involved [16]. In complex alloys, this approach is necessary because the machining performance of the alloys is influenced by a combination of solidification-derived parameters (e.g., liquidus isotherm velocity, cooling rate, dendritic and lamellar spacings, and intermetallic morphology) that interact in a non-linear and interdependent manner. By applying multivariate regression, it becomes possible to quantify the relative importance of each parameter, identify the most statistically significant predictors, and understand the synergistic or antagonistic effects among variables. This statistical modeling provides a more accurate and integrated assessment of the factors controlling machinability, enabling a deeper comprehension of the relationship between solidification characteristics and cutting performance for complex multicomponent alloys

Although extensive studies have addressed the machinability of binary and ternary Al alloys, no recent investigations (last five years) were found focusing on quaternary or higher-order Al-Cu-based alloys containing elements such as Ni and Ta. This lack of studies highlights the scientific gap that the present work aims to fill.

In this context, the present work aims to evaluate the machinability of the Al-33%Cu-1%Ni-1.2%Ta alloy, produced by directional solidification under transient conditions, using four distinct criteria: cutting temperature, tool wear, surface roughness, and chip morphology. This study highlights the inherent complexity in assessing the machinability of alloys containing high amounts of intermetallics, particularly complex ones. The

coexistence of phases with distinct chemical compositions, morphologies, and hardness levels leads to highly non-linear interactions with the cutting tool. These interactions affect cutting temperature, tool wear, surface roughness, and chip formation in different ways. Hard intermetallics, brittle phases, and mismatched constituents can simultaneously trigger adhesive, abrasive, and diffusive wear mechanisms, whose prevalence varies during machining. When multiple machinability criteria are evaluated, the results often reveal conflicting trends, such as microstructures that improve surface finish but accelerate tool wear. This scenario demands a rigorous, multidimensional approach that correlates microstructural features with local physical and thermal properties and process parameters, enabling a comprehensive interpretation of machinability behavior in complex alloys.

II. Materials and Methods

The summary of the development steps of this work is contained in Fig. 1.

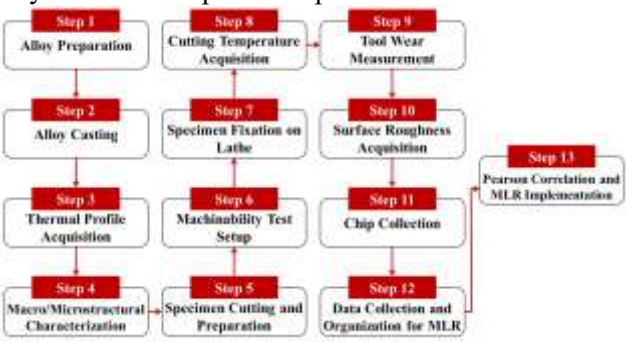

Figure 1. Summary of the development steps of this work.

Alloy Preparation and Solidification Procedure

The experimental material used in this study was an Al-33%Cu-1%Ni-1.2%Ta alloy, produced from commercially pure aluminum, copper, nickel, and tantalum [6, 7]. The charge was weighed to achieve the target composition and melted in a graphite crucible using an electric resistance furnace. The molten alloy was poured into a vertical upward directional solidification device with a water-cooled chill at the bottom, designed to promote unidirectional heat extraction along the length of the casting, as shown in Fig. 2. The process was conducted under transient heat-flow conditions. Casting temperature was monitored by *K*-type thermocouples positioned along the mold axis and connected to a high-precision data acquisition system.

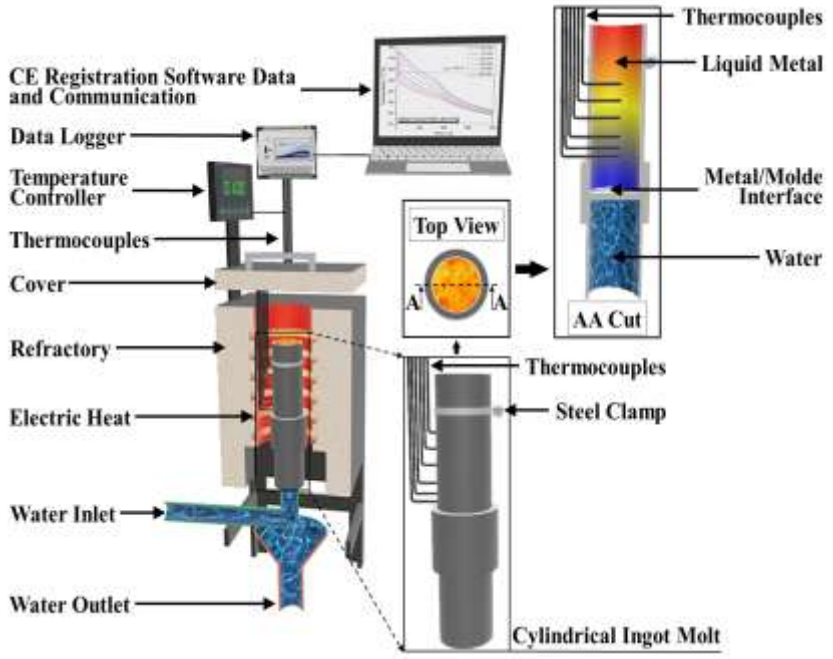

Figure 2. Unidirectional solidification device, highlighting the mold and the cooling system [7].

Detailed descriptions of the alloy preparation, melting, pouring, and solidification procedures, including the setup of the directional solidification device, thermocouple arrangement, and data acquisition methodology, can be found in the literature [7, 6].

Thermal Analysis and Microstructural Characterization

Thermal parameters, including cooling rate (T_R) and liquidus isotherm velocity (V_L), were determined from thermocouple readings following standard procedures (Fig. 3 (a)). After complete solidification, the ingot was sectioned longitudinally (Fig. 3 (b)). Samples were taken at specific distances from the heat-extracting surface to represent different thermal conditions. Specimens were ground with SiC papers (60 to 600 mesh) and polished with alumina suspensions. Chemical etching ($HF\text{-}HNO_3\text{-}HCl\text{-}H_2O$) revealed the microstructure. Macrostructural analysis used stereomicroscopy; microstructural features such as secondary dendritic arm spacing (λ_2) and intermetallic measurements were quantified by optical microscopy and image analysis (Fig. 3 (c)). Fig. 3 shows schematic presentation of these procedures.

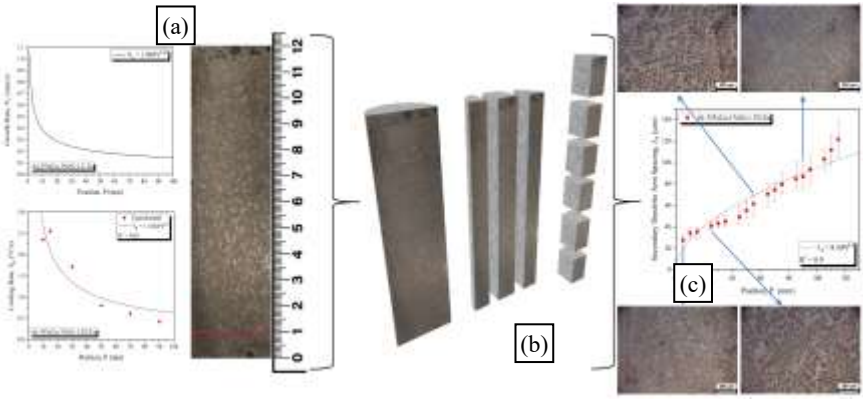

Figure 3. (a) representation of longitudinal and transversal sections for sample extraction, (b) experimental growth and cooling rate with macrostructure and position of the ingot; (c) microstructures and measurements of the spacing of the arms of the secondary dendrites.

Further methodological details on thermal parameter determination, macro/microstructural preparation, and quantitative analysis are provided in [7, 6].

Machinability Testing Procedure

Following the alloy production and solidification stage, the ingot was removed from the mold and sectioned longitudinally. One of the resulting halves was further subdivided into three pieces. This process yielded a rectangular-section specimen with an approximate cross-sectional area of 100 mm² and a length of 120 mm, prepared under continuous water cooling to prevent microstructural alteration or residual stress induction.

The machinability tests were carried out on a *MANROD MR*-320 semi-automatic bench lathe, using dry parting-off operation (also known as cut-off turning) to maximize the severity of cutting conditions and ensure the entire cutting edge was continuously engaged. High-speed steel (*HSS*) tools were used with their factory-ground edges, ensuring consistent tool geometry across tests. Cutting parameters were fixed at a spindle speed of 650 rpm, feed rate of 0.126 mm/rev (automatic), and cutting speed of 28.39 m/min.

A conventional automatic lathe ensures robust repeatability of feed and spindle speed, reflecting standard industrial practice [8,17]. High-speed steel (*HSS*), operating at moderate speeds, is deliberately more thermally sensitive than coated carbides, making it an effective “probe” for detecting microstructures rich in hard, brittle intermetallics [18]. Dry cutting is not only environmentally friendlier but also isolates material-tool interactions

from coolant influences, which significantly affect heat partitioning and wear mechanisms (e.g., elimination of coolant waste, reduced hazardous exposure, and lower emissions) [19].

Cutting positions corresponded to the six thermocouple locations embedded during the alloy's directional solidification from the chilled surface, enabling correlation between solidification thermal parameters, microstructural features, and machinability indicators. The specimen geometry was not modified prior to machining to avoid thermal or mechanical alterations.

Cutting temperature was measured using a non-contact infrared thermometer mounted on a tripod, positioned to capture the tool-chip-workpiece interface temperature in real time [13, 20, 10,11, 8, 9, 12, 21, 7, 14] (Fig. 4).

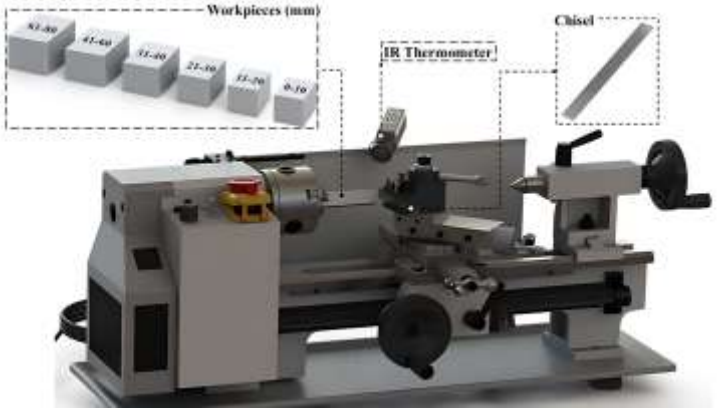

Figure 4. Schematic representation of the bench lathe showing the necking positions, the infrared thermometer and the high-speed steel chisels [13].

Fig. 5 (a) shows the temperature profile for rectangular samples during both intermittent and continuous cutting regimes. At first, contact between the tool and the rectangular sample is intermittent, as the edges interact with the cutting edge. With advancement, the cutting becomes continuous, leading to greater contact between the tool and the sample. As a result, the cutting temperature increases until the process is completed. The infrared thermometer (Fig. 5 (b)) recorded the apparent temperature (T_{ap}) of the observed surface, not the real cutting temperature (T_{rc}). A conversion was therefore required to estimate the actual cutting temperature during machining. To perform this conversion, the emissivity of the investigated

alloy was determined following a procedure similar to that described by [22], in which the global emissivity is expressed mathematically as:

$$\varepsilon_{alloy} = \sum_{i=1}^{n} w_i \times \varepsilon_i \quad (1)$$

where n is the number of alloying elements, ε_i is the emissivity of the pure element i, w_i is its mass fraction (%), and ε_{alloy} is the overall alloy emissivity. For the present alloy (Al-33%Cu-1%Ni-1.2%Ta, the calculated emissivity was ε_{alloy} = 0.46.

The conversion to real cutting temperature values was made using the radiation energy equation [12,13]:

$$T_{rc} = T_{ap} \times \sqrt[4]{\frac{\varepsilon_{ap}}{\varepsilon_{alloy}}} \quad (2)$$

where ε_{ap} is the apparent emissivity set in the infrared thermometer. This conversion was applied to all temperature readings obtained during the tests. These corrected values were then used in the calculation of the heating rate, a parameter directly dependent on the thermal energy generated during the cutting process. The heating rate (T_{aq}) for each cut was calculated as the slope between the initial and maximum temperatures during continuous cutting, as shown in Fig. 5.

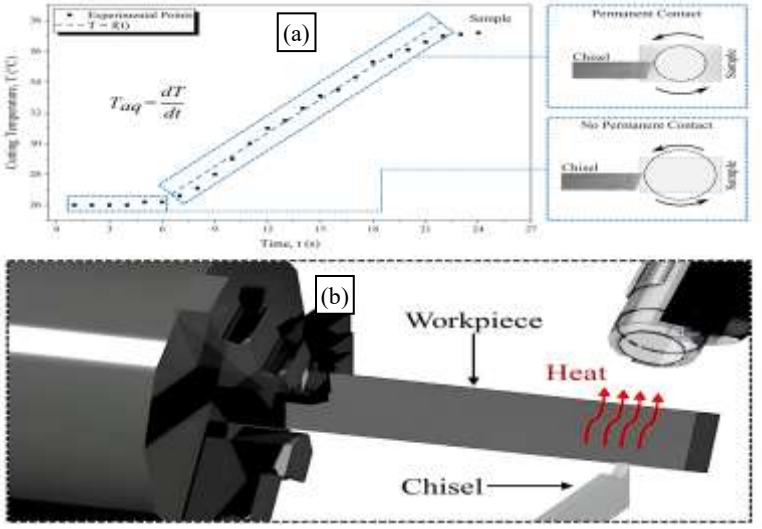

Figure 5. Schematic representation of the setup used in the machinability tests, showing (a) technique used to calculate the heating rate; (b) workpiece features, position of chisel and infrared thermometer. Adapted from [11].

Tool wear was quantified following *ISO* 3685: 2017 [23], adopting the maximum flank wear (VB_{max}) as the tool life criterion (Fig. 6 (a)). For each

parting tool used in the tests, high-resolution images of the cutting edge were obtained via stereomicroscopy, as shown in Fig. 6 (b). The images were processed and analyzed in the ImageJ® software, following the methodology already described in the literature [13, 8, 10, 24].

Surface roughness was assessed through a non-contact image correlation technique, which eliminates potential interference from stylus-based profilometers in irregular or discontinuous surfaces. After each cut, the machined surface was sectioned according to the pre-established thermal mapping positions and further divided into four quadrants. This division allowed stereomicroscopy imaging of each quadrant at high magnification, ensuring that localized variations in surface topography were adequately represented (Fig. 6 (c)). The captured images were later processed using ImageJ® software analysis routines to extract roughness parameters such as *Ra* and *Rz*, enabling a quantitative evaluation of surface quality across all tested conditions. This procedure is already found in the literature [13, 11, 25, 26].

Chip morphology analysis was conducted immediately after each cut to prevent oxidation or deformation of the samples. Chips were collected individually in a clean stainless-steel tray positioned directly beneath the cutting zone. The tray was thoroughly cleaned after each trial to avoid cross-contamination between samples. The collected chips were dried, stored in labeled containers, and subsequently examined under stereomicroscopy to characterize their geometry, segmentation pattern, and surface features (Fig. 6 (d)) [27].

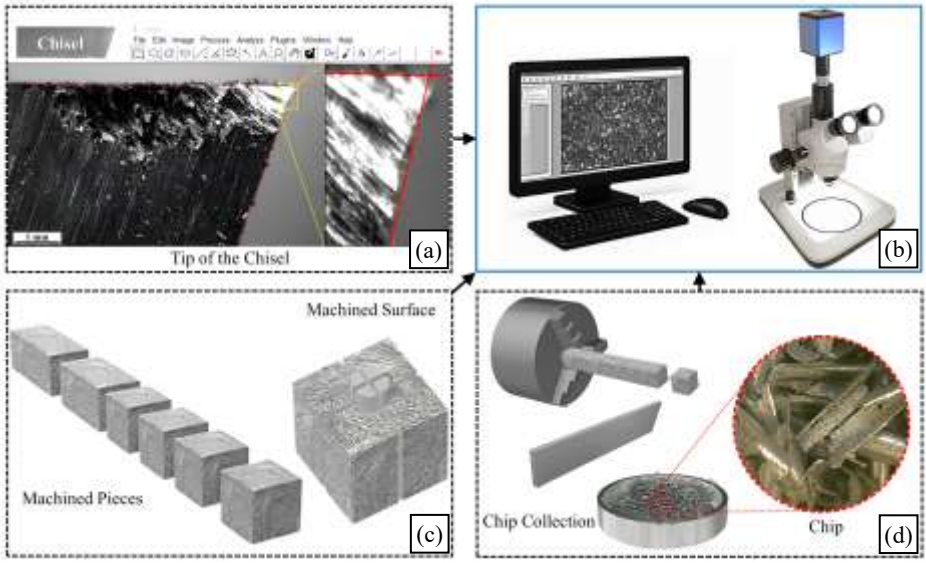

Figure 6. (a) surface roughness divided into four quadrants; (b) stereomicroscopy; (c) tool wear; (d) chip morphology analysis.

Data Treatment and Statistics

For the application of Multiple Linear Regression (*MLR*), a database was compiled containing the independent (green, in Fig. 7) and dependent variables (red, in Fig. 7) related to the solidification experiment and machinability tests.

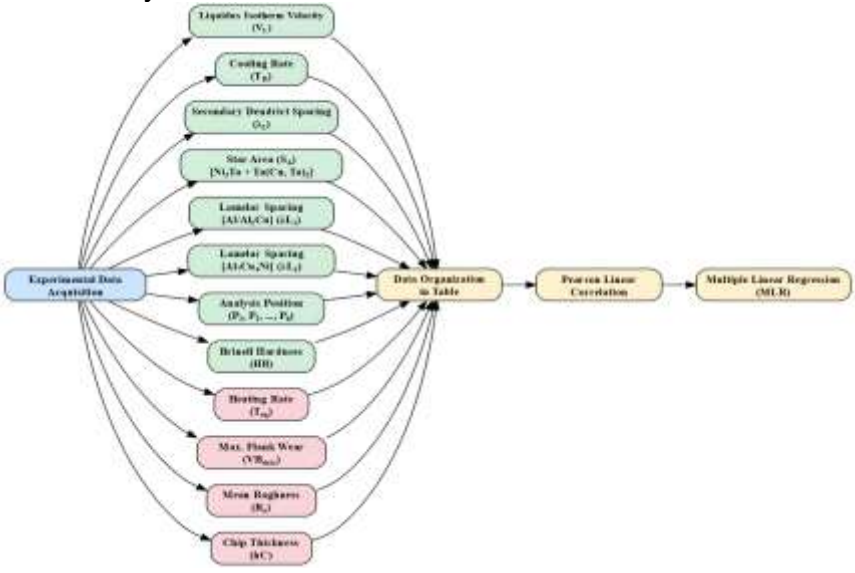

Figure 7. Data structure for Multiple Linear Regression.

Initially, the independent parameters obtained experimentally were defined, including:

- Liquidus isotherm velocity (V_L, mm/s) - determined from the thermal records acquired during solidification, by analyzing the variation in the isotherm position over time.
- Cooling rate (T_R, °C/s) - calculated from the derivative of the cooling curve in the interval immediately after the passage of the liquidus isotherm.
- Secondary dendritic arm spacing (λ_2, μm) - measured in metallographic samples using image analysis software, considering the average of multiple measurements in representative regions.
- Star-shaped area (SA, μm²) - associated with the intermetallic phase Ni_3Ta + $Ta(Cu,Ta)_2$, determined through segmentation and quantification of areas in the microstructure.
- Al/Al_2Cu lamellar spacing (λL_1, μm) - obtained by image analysis at the appropriate magnification, measuring the average distance between lamellae.
- Al_7Cu_4Ni lamellar spacing (λL_2, μm) - measured similarly to λL_1.
- Analysis positions (P_1 to P_6) - corresponding to different distances from the cooled end, expressed in millimeters.
- Brinell hardness (HB) - measured with standardized load and indenter, considering the average of three impressions per position.
  The dependent variables were defined as the machinability criteria, comprising:
- Heating rate (T_{aq}, °C/s) - obtained from the linear slope in the cutting temperature rise stage.
- Maximum flank wear (VB_{max}, mm) - measured in accordance with *ISO* 3685 by optical microscopy imaging of the cutting edge.
- Average surface roughness (Ra, μm) - determined through image correlation of the machined surface, subdivided into quadrants for improved sampling.
- Chip thickness (h_C, mm) - measured directly using a digital caliper on chips collected immediately after cutting.
  All data were organized into a table, in which each analysis position (*P1* to *P6*) was associated with the corresponding values of the independent and dependent variables.

After data organization, Pearson's linear correlation analysis was performed to quantify the degree of association between each independent

variable and the machinability criteria, identifying directly proportional (positive correlation) and inversely proportional (negative correlation) relationships.

Finally, the Multiple Linear Regression model was implemented to identify the independent variables with the greatest statistical significance for each machinability criterion, thus allowing inference of which microstructural and thermal parameters exert the most influence on the cutting performance of the studied alloy.

Uncertainty and Quality Control

Instrumentation accuracies were considered in uncertainty budgets (*IR* thermometer ±(1% reading + 1 °C); microscope scale calibration ±1-2%). Tool geometry was checked with a toolmaker's microscope after grinding. The test order across positions P was randomized to mitigate drift effects. Environmental conditions (room temperature, airflow) were kept constant during thermal measurements.

III. Results and Discussion

Solidification, Macro/microstructure, Intermetallic Evolution, and Hardness

The following results from solidification kinetics, macro/microstructure, and intermetallic evolution are a compilation of the studies by [6] and [7].

Al-33%Cu-1%Ni-1.2%Ta ingot solidified under upward transient directional cooling exhibited the expected monotonic decay of solidification kinetics with distance from the chill, as shown in Fig. 8. According to the same figure, the macrography revealed a fine columnar zone extending ~10 mm from the chill, followed by a mixed columnar-equiaxed region up to ~ 45 mm, and a fully equiaxed zone thereafter. Microstructural and *SEM-EDS* analyses converge to a coherent formation pathway for the quaternary intermetallic population under non-equilibrium, transient cooling. In early (high-T_R) positions, α-Al dendrites solidify with limited interdendritic precipitation; the first intermetallics detected are Al_3Ta and θ-Al_2Cu. As T_R decreases along the ingot, time for diffusion increases and complex, Ta- and Ni-bearing compounds nucleate and grow in the interdendritic channels: diamond/rhomboid-shaped particles identified as Ni_3Ta and $Ta(Cu,Al)_2$ appear, often surrounded by a lamellar eutectic. With further reduction in T_R, these complex particles are progressively consumed at their "edges," giving rise to an Al_7Cu_4Ni rim, while the surrounding eutectic becomes pronounced. This sequence

($Al_3Ta \rightarrow (\alpha\text{-}Al + Al_2Cu) \rightarrow \{Ni_3Ta + Ta(Cu,Al)_2\} \rightarrow Al_7Cu_4Ni$ rims) matches the observed mapping of Al-rich dendrites and interdendritic enrichment in Cu, Ni, and Ta. It rationalizes the strong position-dependent contrast between early refined morphologies and late coarse eutectic/intermetallic networks.

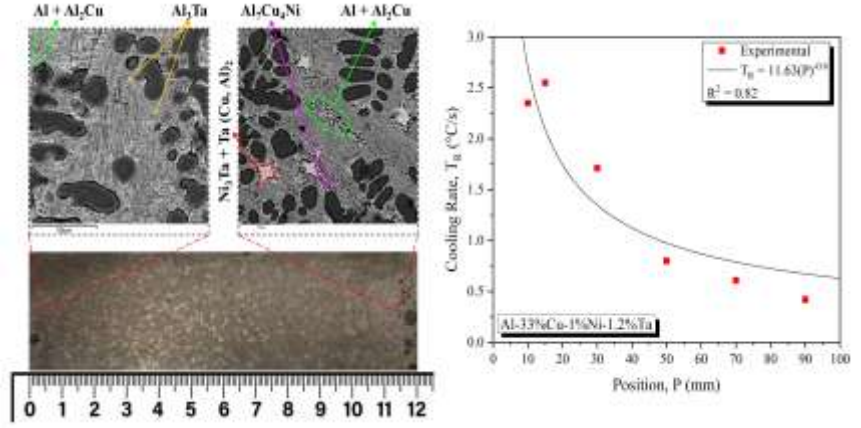

Figure 8. Influence of the cooling rate on peritectic reactions and morphology of the Al-33%Cu-1%Ni-1.2%Ta alloy structure [7].

According to Fig. 9, progressing away from the chill, λ_2 increased systematically with position, reflecting the longer local solidification times under weaker heat flow. Complementary measurements targeting the eutectic/intermetallic scales demonstrate that thermal history does not affect all phases equally. The lamellar spacing of the Al/Al_2Cu eutectic (λL_1), the area of the star-shaped complex intermetallic ($Ni_3Ta + Ta(Cu,Al)_2$), and the lamellar spacing of the Al_7Cu_4Ni-bearing eutectic (λL_2) were systematically extracted. The star area decreases as T_R increases (i.e., complex particles are suppressed by faster cooling), whereas λL_1 increases with T_R, a trend opposite to binary Al-Cu eutectics, highlighting the peritectic reactions and solute partitioning unique to the multicomponent system. In contrast, λL_2 remains approximately insensitive to T_R within experimental scatter, suggesting a comparatively narrow kinetic window for that eutectic's selection.

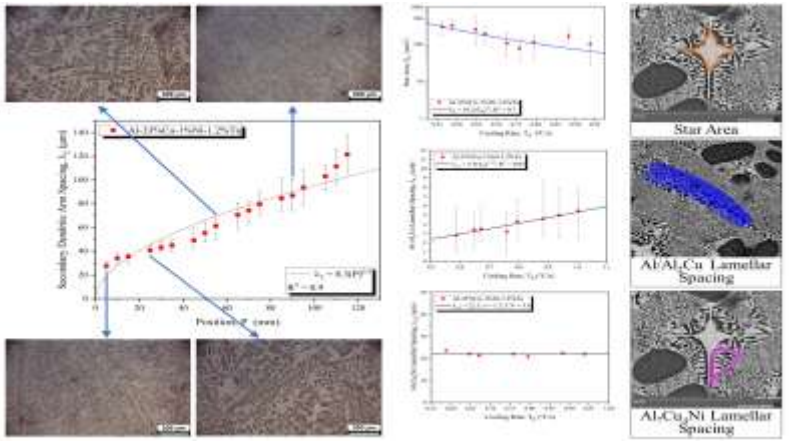

Figure 9. Variation of secondary dendritic spacings with ingot position and some microstructures observed along the ingot; area of the star as a function of the cooling rate; Lamellar spacing of the Al-Al2Cu intermetallic as a function of the cooling rate; Lamellar spacing of the Al7Cu4Ni intermetallic as a function of the cooling rate. Adapted from [6], [7].

Fig. 10 shows that Brinell hardness remained relatively constant along the ingot, with a standard deviation of 25.52 and a coefficient of variation (*CV*) of 18.22%, classified as medium and acceptable. This stability, despite variations in λ_2, results from a compensatory effect. Dendritic refinement is balanced by the presence of hard complex intermetallics, offsetting the expected hardness reduction in coarser regions.

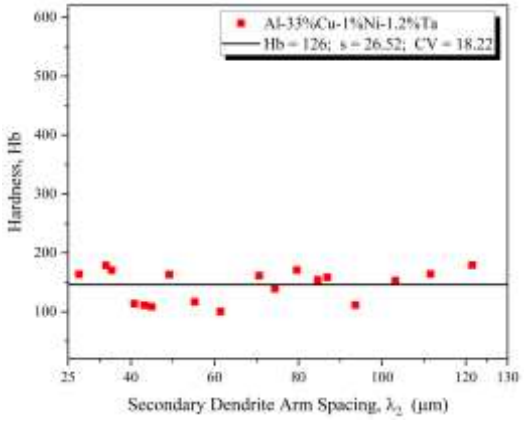

Figure 10. Brinell hardness as a function of secondary dendrite arm spacing.

Integrated Picture and Implications for Machinability

Taken jointly, the thermal map → *CET* → λ_2 scalings → intermetallic pathway → eutectic metrics describe a tightly coupled solidification landscape for Al-33%Cu-1%Ni-1.2%Ta. Regions nearer the chill (high V_L/T_R) combine refined λ_2 and limited intermetallic development, whereas distal regions (low V_L/T_R) exhibit coarse λ_2, abundant θ-Al_2Cu lamellae, robust Ni_3Ta/$Ta(Cu,Al)_2$ particles with Al_7Cu_4Ni rims and pronounced eutectic networks. Because intermetallic hardness, morphology (diamond-like facets vs. lamellae), and spatial distribution govern local thermal conductivity, chip formation, and tool-work tribology, these gradients are expected to translate into position-dependent machinability—even under fixed cutting conditions. The next subsection leverages these solidification-microstructure baselines to interpret measured cutting temperature, chip thickness, flank wear, and surface roughness across the mapped positions.

Machinability Results

Cutting temperature is strongly influenced by cutting speed, feed rate, the use or absence of cutting fluid, the rigidity of the machine-tool system, and the microstructural characteristics of the material [13, 20, 10, 11, 8, 9, 12, 21, 7, 14]. In the present study (Fig. 11 (a)), the highest temperature was recorded at position *P4* (40 mm from the cooled end), while *P1-P3* exhibited lower values. The highest temperatures occurred during shorter cutting durations. This suggests that the alloy's low thermal conductivity, together with complex intermetallic phases, promotes heat retention in the cutting zone.. As reported by [28] and [29] and [1], increases in λ_2 and higher fractions of complex intermetallics reduce thermal conductivity and hinder heat dissipation, raising local temperatures and potentially intensifying thermal wear mechanisms.

The heating rate, also in Fig. 11 (b), displayed an oscillating behavior along the ingot, differing from the monotonic profiles reported in [12] and [14]. This oscillation correlates with the extent of the columnar-to-equiaxed transition (*CET*), identified between 10 and 45 mm from the cooled end [6]. Within this region, microstructural heterogeneity generates local variations in both thermal conductivity and mechanical resistance, affecting heat generation and dissipation during cutting.

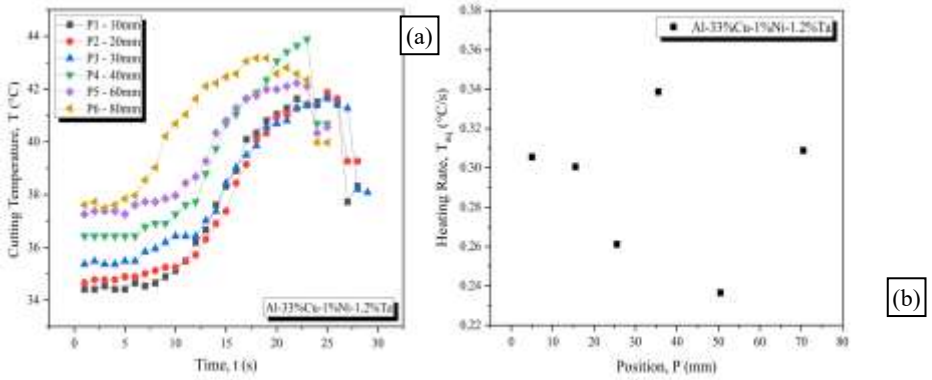

Figure 11. (a) cutting temperatures as a function of time; (b) machining heating rate as a function of position for the analyzed experiments.

Tool Wear

Tool wear was predominantly characterized by flank wear with material adhesion (Fig. 12 (a)), indicative of an adhesive wear mechanism, which was already discussed in the literature [30, 31, 13, 8, 10, 24]. The maximum recorded wear (0.071 mm, tool 2) was significantly below the ISO 3685 limit (VB_{max} = 0.6 mm), indicating that the cutting conditions and overall material hardness allowed for a satisfactory tool life. The highest wear rate occurred at the 15 mm position (Fig. 12 (b)), located within the CET region. This increase is due to heterogeneous microstructures and a greater presence of hard, abrasive intermetallics (Ni_3Ta, Al_7Cu_4Ni). These particles act as localized wear points on the cutting edge.

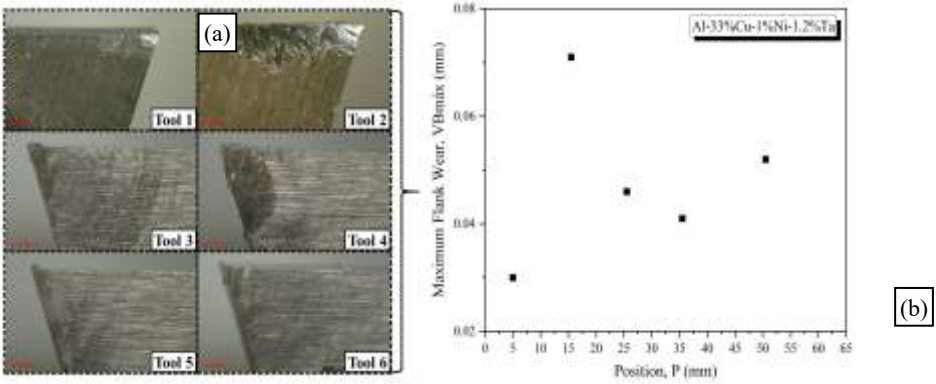

Figure 12. (a) cutting tools after testing; (b) maximum flank wear as a function of position.

Surface Roughness

From the surface of the pieces (Fig. 13 (a)), the average surface roughness (Fig. 13 (b)) was highest in the initial region (~ 0.27 μm), decreased to ~ 0.20 μm between 10 and 35 mm, and further dropped to ~0.17 μm between 50 and 70 mm. This behavior reflects the macrostructural evolution of the ingot: the refined columnar region at the cooled end tends to generate more stable chips but with higher cutting energy and vibration, leading to increased roughness; in the *CET* region, microstructural heterogeneity causes small roughness fluctuations; in the equiaxed region, the more homogeneous phase distribution and greater spacing between hard particles contribute to improved surface finish.

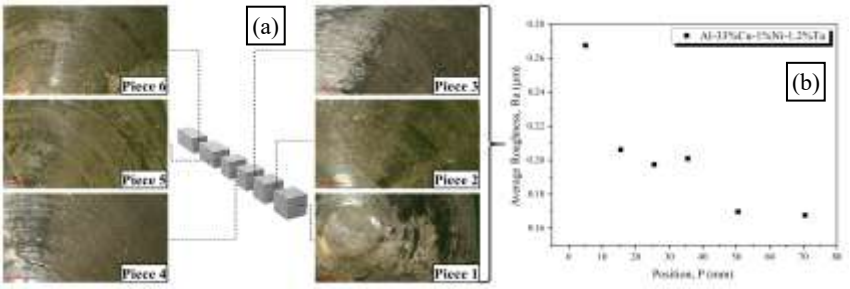

Figure 13. (a) surface of the pieces; (b) average surface roughness.

Chip

The chips obtained (Fig. 14 (a)) exhibited short morphologies, predominantly arc- and needle-shaped. Arc-shaped chips prevailed in the initial regions, where λ_2 is smaller and the fraction of complex intermetallics is lower, favoring more uniform shearing. In the *CET* and equiaxed regions, a coexistence of arc and needle morphologies was observed, associated with a higher presence of complex intermetallics that intensify chip segmentation and promote premature fracture during shearing. This fragmentation reduces chip length, decreasing the contact area with the tool and, consequently, abrasive wear (Fig. 14 (b)).

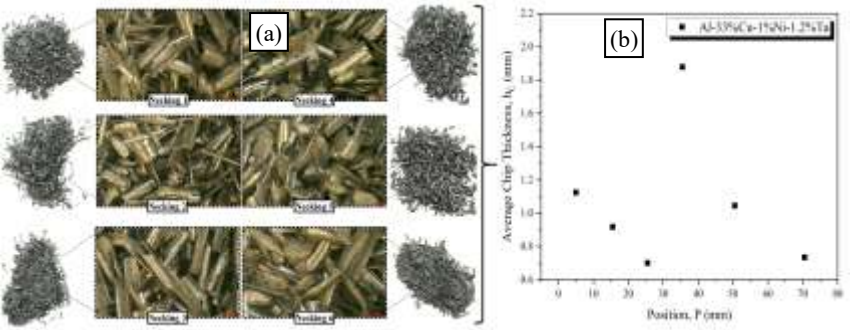

Figure 14. (a) chip morphology; (b) average chip thickness as a function of position.

Multiple Linear Regression

The Multiple linear regression analysis (Fig. 15) revealed that the liquidus isotherm velocity (V_L) was the most influential variable on all machinability criteria, followed by cooling rate (T_R). Higher V_L and T_R values, associated with finer microstructures, increased the mechanical strength of the matrix, which in turn elevated wear, heating rate, roughness, and chip thickness. The Al/Al_2Cu phase exhibited a reducing effect on wear, roughness, and chip thickness due to its less abrasive nature and its ability to act as a mechanical "buffer" in the tool-workpiece contact. Conversely, λ_2 had a positive but less pronounced effect on machinability criteria, reflecting its indirect influence through modifications in intermetallic morphology and distribution.The constant results were excluded from the multivariate regression analysis because variables with no variation across the experimental dataset do not contribute to the statistical modeling of relationships between predictors and responses. In regression, the effect of a variable is estimated based on changes in its value; when a variable remains constant, its variance is zero, making it impossible to compute meaningful regression coefficients. Including such variables can also introduce computational redundancy without improving model fit or explanatory power. Therefore, although parameters such as hardness are relevant to the process physics, their effects are implicitly accounted for in the other results.

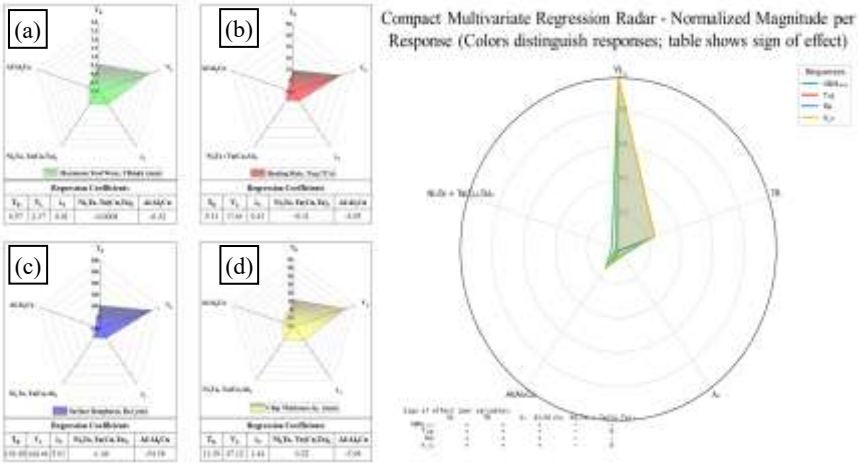

Figure 15. Multivariate regression plots for machinability responses: (a) maximum tool wear (VB_{max}), (b) heating rate (T_{aq}), (c) surface roughness (R_a), and (d) chip thickness (h_C), as a function of the independent variables

T_R, V_L, λ_2, Al/Al_2Cu, and Ni_3Ta + $Ta(Cu,Ta)_2$. On the right, radar chart with normalized magnitude per response and a table indicating the sign of effect for each variable.
In summary, thermal and structural variations along the ingot directly affect machinability behavior, with the *CET* region representing the most critical zone due to its microstructural heterogeneity and high fraction of hard phases, which increase wear and thermal instability.

IV. Conclusions

The present work established a clear correlation between solidification thermal parameters, microstructural evolution, and machinability behavior in the Al-33%Cu-1%Ni-1.2%Ta alloy, produced under upward transient directional solidification. The mapping of cooling rate, dendritic spacing, intermetallic morphology, and hardness across the ingot provided an integrated picture of how solidification history dictates mechanical response during cutting.

The columnar-to-equiaxed transition (*CET*) region was identified as the most critical zone for machinability. Here, microstructural heterogeneity, with a high fraction of hard, complex intermetallics (Ni_3Ta, $Ta(Cu,Al)_2$, and Al_7Cu_4Ni rims), increased flank wear and thermal instability, despite overall hardness remaining constant due to a compensatory effect between dendritic refinement and intermetallic abrasiveness. This stability in hardness, even with significant λ_2 variation, is a novel observation for this alloy system and underscores the interplay between phase morphology and mechanical resistance.

Multivariate regression revealed that liquidus isotherm velocity (V_L) and cooling rate (T_R) were the dominant parameters affecting all machinability criteria. Finer microstructures, promoted by higher V_L/T_R, increased matrix strength and, consequently, wear, heating rate, roughness, and chip thickness. The Al/Al_2Cu phase played a beneficial role by reducing wear and roughness through its less abrasive nature, while the effect of λ_2 was indirect and linked to modifications in intermetallic distribution.

Scientifically, this research fills a gap by quantifying how multicomponent intermetallic networks, formed through non-equilibrium solidification pathways, influence chip formation, heat generation, and tool-workpiece tribology. From an industrial perspective, the results provide practical guidelines for optimizing machining strategies and controlling thermal gradients during solidification, allowing for improved tool life, better

surface quality, and more predictable performance in the manufacturing of components from complex aluminum alloys.

Acknowledgment
The authors would like to acknowledge the financial support provided by the National Council for Scientific and Technological Development (*CNPq*) and the Coordination for the Improvement of Higher Education Personnel (*CAPES*), Brazil. We are also grateful to the Federal University of Pará (*UFPA*) and the Federal Institute of Pará (*IFPA*) for the research infrastructure, laboratory facilities, and institutional support that made this work possible.

References
1. S. Li, X. Yue, Q. Li, H. Peng, B. Dong, T. Liu, H. Yang, J. Fan, S. Shu, F. Qiu, Q. Jiang: J Mater Res Technol, 23 (2023) 9262-9289.
2. E. Georgantzia, M. Gkantou, G. Kamaris: Eng Struct, 234 (2021) 111372.
3. S. Shamsudin, M. Lajis, Z. Zhong: Proc CIRP, 40 (2016) 256-261.
4. X. Fang, Y. Li, Q. Zheng, J. Guo, Y. Yang, W.C. Ding, K. He, N. Su, J. Jiang, X. Chen, H. Wang: Metals, 12 (2022) 2178.
5. A. Barros, C. Cruz, A. Silva, N. Cheung, A. Garcia, O. Rocha, A. Moreira: Corros Eng Sci Technol, 55 (2020) 1-9.
6. W. Jesus, V. Silva, H. Souza, T. Costa, O. Rocha, L. Nascimento, A. Silva: Trends Sci, 21 (2024) 1-12.
7. V. Silva, W. Jesus, A. Maciel, L. Nascimento, H. Alkimim, E. Lima, A. Silva: Rev Contemp, 5 (2025) e7660.
8. C. Silva, L. Leal, E. Guimarães, P. Júnior, A. Moreira, O. Rocha, A. Silva: Adv in Mater Sci Eng, 1 (2018) 9512957.
9. A. Silva, I. Silva, J. Barros, C. Silva, O. Rocha: Defect and Diffus Forum, 365 (2015) 116-121.
10. J. Nascimento, R. Barros, C. Konno, A. Silva, O. Rocha, A. Moreira: Period Tche Quim, 16 (2019) 860-874.
11. T. Costa, M. Dias, C. Silva, E. Freitas, A. Silva, N. Cheung, A. Garcia: Int J Adv Des Manuf Technol, 108 (2020) 1-12.
12. S. Silva, J. Filho, C. Santos, T. Costa, O. Rocha, A. Silva: Braz J Dev, 7 (2021) 60959-60971.
13. A. Maciel, A. Gatinho, C. Brabo, A. Silva, S. Maues, N. Cosmo, O. Rocha, A. Silva: Peer Review, 5 (2023) 355-374.
14. S. Maués, A. Maciel, A. Silva, H. Souza, N. Cosmo, A. Vasconcelos, A. Silva: Peer Review, 6 (2024) 345-364.
15. M. Phate, A. Bendale, S. Toney, V. Phate: Heliyon, 6 (2020) e05308.

16. Y.L. Tchigirinsky, N.V. Chigirinskaya, Z.S. Tikhonova, In: Proceedings of the 6th International Conference on Industrial Engineering (ICIE 2020). Eds.: A.A. Radionov, V.R. Gasiyarov. Cham, Springer International Publishing 2021, pp. 1101-1108.
17. R. Subarkah, G. Heryana, K. , M. Sholeh, F. Zainuri, C. Widiawaty: IOP Conf Ser: Mater Sci Eng, 1034 (2021) 012101.
18. A. Chaus, A. Kryshtal: Mater Charact, 203 (2023) 113313.
19. T. El-Hossainy: Mater Manuf Processes, 16 (2001) 165-176.
20. A. Maciel, N. Cosmo, H. Souza, S. Maués, A. Farias, A. Vasconcelos, O. Rocha, A. Silva: Curr Trends Eng Sci, 3 (2023) 1047.
21. A. Botelho, P. Junior, M. Silva, R. Silva, A. Nascimento: Period Tche Quim, 16 (2019) 440-449.
22. N. Amoafo-Yeboah, A. Rabiei: J Compos Sci, 8 (2024) 202.
23. ABNT: NBR ISO 3685 - Ensaios de vida da ferramenta de ponta única para torneamento, (2017) 69.
24. P. Junior, G. Figueiredo, T. Costa, J. Silva, T. Botelho, R. Pinto, A. Silva: Braz J Dev, 8 (2022) 5997-6006.
25. T. Costa, G. Figueiredo, J. Silva, R. Pinto, P. Junior, T. Botelho, O. Rocha, A. Silva: Curr Trends Eng Sci, 3 (2023) 1028.
26. T. Botelho, A. Maciel, F. Rocha, J. Nascimento, A. Silva: Cuad Educ Desarro, 15 (2023) 1600-1610.
27. Y. Gao, R. Sun, Y. Chen, J. Leopold: Int J Mec Sci, 111 (2016) 88-100.
28. F. Stadler, H. Antrekowitsch, W. Fragner, H. Kaufmann, E. Pinatel, P. Uggowitzer: Mater Sci Eng A, 560 (2013) 481-491.
29. A. Zhang, Y. Li: J Mater Res, 38 (2023) 2049-2058.
30. M. Ponce, I. Illana, S. Fernandez-Vidal, J. Gomez: Materials, 11 (2018) 1598.
31. N. Raof, N. Daud, A. Aziz, A. Ghani, A. Dahnel, S. Mokhtar, N. Khairussaleh: IIUM Eng J, 21 (2020) 177-185.